

# The discrepancy in G-band contrast: Where is the quiet Sun?

H. Uitenbroek, A. Tritschler and T. Rimmele

*National Solar Observatory/Sacramento Peak<sup>1</sup>, P.O. Box 62, Sunspot, NM-88349, U.S.A.*

`huitenbroek@nso.edu, ali@nso.edu, trimmele@nso.edu`

Version November 15, 2018

## ABSTRACT

We compare the rms contrast in observed speckle reconstructed G-band images with synthetic filtergrams computed from two magneto-hydrodynamic simulation snapshots. The observations consist of 103 bursts of 80 frames each taken at the Dunn Solar Telescope (DST), sampled at twice the diffraction limit of the telescope. The speckle reconstructions account for the performance of the Adaptive Optics (AO) system at the DST to supply reliable photometry. We find a considerable discrepancy in the observed rms contrast of 14.1% for the best reconstructed images, and the synthetic rms contrast of 21.5% in a simulation snapshot thought to be representative of the quiet Sun. The areas of features in the synthetic filtergrams that have positive or negative contrast beyond the minimum and maximum values in the reconstructed images have spatial scales that should be resolved. This leads us to conclude that there are fundamental differences in the rms G-band contrast between observed and computed filtergrams. On the basis of the substantially reduced granular contrast of 16.3% in the synthetic plage filtergram we speculate that the quiet-Sun may contain more weak magnetic field than previously thought.

*Subject headings:* Sun: granulation — Sun: photosphere — techniques: high angular resolution — (magnetohydrodynamics:) MHD

## 1. Introduction

Magneto-hydrodynamic simulations are increasingly successful in reproducing the observable effects of magneto-convection on the solar surface. In achieving this goal they provide not only

---

<sup>1</sup>Operated by the Association of Universities for Research in Astronomy, Inc. (AURA), for the National Science Foundation

insight into the physics that drives convective patterns at the surface, but also into the dynamics of the solar interior, where at best only helioseismological observations can probe. Although the simulations are typically claimed to be parameter free, and therefore cannot be adjusted at will to match observations, they include arbitrary elements in the choice of the physical approximations that are implemented to keep the numerical problem tractable. Significant limitations are restricting radiative transfer to a small number of representative frequency bins and discrete directions, and strongly reducing the Reynolds numbers in the simulation to values that are orders of magnitude less than in reality (Stein & Nordlund 1998; Vögler et al. 2005; Schaffenberger et al. 2006). The latter restriction limits the smallest spatial scales at which structures can occur and how the dynamics on these scales can possibly feed back to larger scales.

One of the major successes of solar convection simulations is the very accurate reproduction of spatially and temporally averaged shapes of weak photospheric lines (Asplund et al. 2000b; Stein & Nordlund 2000). These line shapes, characterized by an asymmetry towards the blue, are the intricate product of correlation between up- and downflows, and their respective brightness differences and area asymmetries. Because the comparison is made on the basis of spatially and temporally averaged profiles spatial resolution in the observations is irrelevant. This is not true for the numerical resolution, which needs to be sufficiently refined to provide a good match to observed average line profiles (Asplund et al. 2000a). However, the averaging may mask discrepancies in separate quantities, like brightness contrast, velocity variations, and size spectrum of the convective structures that could compensate each other in the averaging process.

In concert with developments in theoretical modeling, a concomitant progress in observational techniques of the solar atmosphere has taken place. In particular, the advent of high order, high temporal bandwidth adaptive optics and post facto image reconstruction techniques, like speckle interferometry (e.g., von der Luehe 1993) and multi-object multi-frame blind deconvolution (e.g., van Noort et al. 2005), have greatly advanced our capabilities of imaging the solar surface with high fidelity. Together these developments should allow for a promising and more realistic comparison between theoretical predictions and observations. Here we attempt to take advantage of developments in instrumentation in order to compare simulations and observations on the basis of only the rms contrast, in particular that in the G band. This eliminates the possible confusion of mixing velocity signatures with intensity contrast that is inherent in the comparison of spatially and temporally averaged line profile shapes, but of course has the drawback that we have to compare with spatially resolved observations. Thus we have to compensate for the image degradation imposed by the Earth’s atmosphere, the telescope, and the instruments on our observed contrast measurements. To accomplish this we employ a speckle reconstruction technique especially adapted to provide a realistic reconstruction of image amplitudes, taking into account the impact of the telescope’s Adaptive Optics (AO) system on the Speckle Transfer Function (STF).

Employing the G band for a comparison between synthetic and observed contrasts has several advantages. Imaging in the band is commonly used in high resolution observations and most observatories nowadays have filters with similar passbands, so that comparisons can be readily made. Secondly, because a typical G-band filter is 1 nm wide (FWHM), it integrates over many lines, masking small uncertainties in individual line positions and averaging out random uncertainties in line strengths. The integrated G-band intensity is also insensitive to Doppler shifts and Zeeman splitting, allowing a comparison of intensity contrast only. The CH molecular lines that dominate the G band form in the photosphere where the approximation of Local Thermodynamic Equilibrium (LTE) applies, which simplifies their numerical modeling. Moreover, the response of the integrated G-band intensity to temperature is dominated by the continuum (Uitenbroek & Tritschler 2006), to which LTE definitively applies.

In their overview of realistic solar convection simulations Stein & Nordlund (2000) compare histograms of granular contrast observed with the 0.5 m Swedish telescope in the continuum with the contrast from their simulations, and find very good agreement after smearing the artificial data with a Point Spread Function (PSF) representative of the telescope and atmosphere. Asensio Ramos et al. (2006) compare the statistics of spatially resolved line profiles of the Fe I 709.0 nm line observed with the Interferometric Bidimensional Spectrometer (IBIS) at the DST with those of profiles computed through a three-dimensional hydrodynamic snapshot, and find very good agreement for the intensity distributions in the continuum (after the theoretical profiles were adjusted for degradation by the telescope and earth atmosphere) and for the correlation between wavelength dependent intensity and intensity in the continuum. However, they also find that the spread in velocities in the simulation is higher than in the observed profiles, with the latter lacking velocities beyond  $\pm 1.2 \text{ km s}^{-1}$ . Keller (2007) provides an overview of the promises and pitfalls of comparing high spatial resolution observations with magneto-hydrodynamic simulations.

In § 2 we introduce the observational details and in § 3 the speckle reconstruction method. The simulations are described in § 4. In § 5 we compare the theoretical and observed G-band contrast. Conclusions are given in § 6.

## 2. Observations

The observations were obtained on October 24, 2005 at the Dunn Solar Telescope (DST) of the National Solar Observatory at Sacramento Peak, Sunspot, taking advantage of the high-order adaptive optics system (Rimmele 2004) and a high-speed  $2\text{k}\times 2\text{k}$  detector with  $12 \mu$  pixels manufactured by DALSA for data acquisition. The optical setup provides a field-of-view (FOV) of about  $61''\times 61''$ . To select the G-band wavelength range a 1.0 nm wide interference filter centered around 430.5 nm located in front of the detector was used. The diffraction limit ( $\lambda/D$ ) of the DST

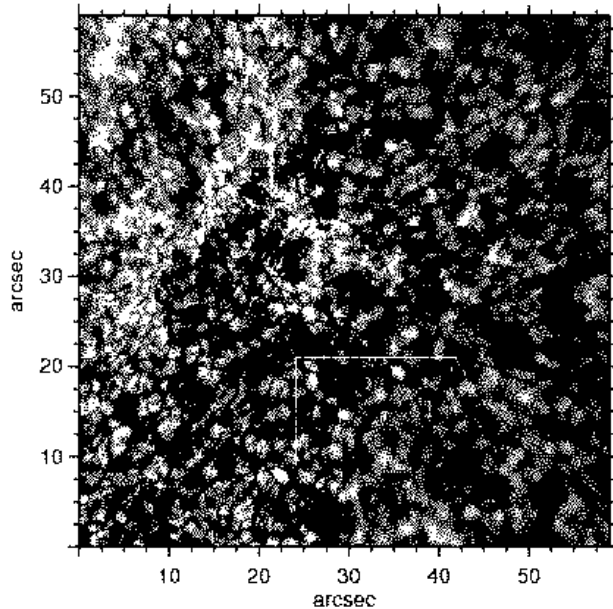


Fig. 1.— Combination of the reference frame (*left half*) and burst average (*right half*) of burst No. 9.

at this wavelength is  $0''.117$  which together with the detector image scale of  $0''.030 \text{ pixel}^{-1}$  leads to an approximate twofold spatial oversampling of four resolution elements of  $\lambda/D$  per pixel, where  $D = 0.76 \text{ m}$  is the aperture of the DST.

### 3. Speckle reconstruction

In order to allow for speckle reconstruction the data was recorded in bursts of 80 images, which were acquired within 3.5 sec and streamed off within 30 sec. The exposure time for an individual frame was 10 ms. The whole data set comprises 103 bursts with a mean cadence of 67 sec, covering a time period of almost 2 h in total. We employ a speckle masking technique, implemented by (Wöger 2007), that incorporates an iterative weighted least-squares fitting method for phase reconstruction and based on a technique by (Matson 1991). In order to get an improved amplitude reconstruction, and thus more reliable photometry, the reconstruction code takes into account how the wavefront correction of the AO system affects the STF.

Each burst frame was divided into  $15 \times 15$  of  $7''.68$  square each. The image was then reconstructed on each subfield individually, after which the corrected subfields were merged back together to give the complete reconstructed frame. A byproduct of the speckle reconstruction code is an estimation of the Fried parameter  $r_0$  over each of the  $15 \times 15$  subfields in the FOV. These

values characterize the atmospheric seeing over the duration of each burst with higher values corresponding to more favorable conditions. The top panel of Figure 2 shows the mean value of  $r_0$  for each burst averaged over the subfields (*solid line and diamonds*) and the standard deviation in the mean (*grey shading*). A histogram of  $r_0$  values per subfield and per burst is shown in the bottom panel of Figure 2. Both panels make clear that the atmospheric seeing conditions were good to very good during most of the 2 h sequence.

The top panel of Figure 3 shows the rms contrast variation of a quiet area just below the pore (indicated by the white rectangle in Figure 1) in all 8240 frames of the 103 bursts. The typical uncorrected rms G-band contrast varies between 5 and 7.5% in these individual frames, very rarely reaching values over 8%. The selected quiet area is close to the AO lock point, which was set at the pore, and is relatively devoid of bright points, and thus is less likely to have strong magnetic fields. The speckle reconstruction algorithm was successful in 101 of the bursts. In these successfully reconstructed images the rms contrast over the same region of quiet Sun is plotted in the bottom panel of Figure 3 (*dashed line with open circles*). An alternative estimate for the quiet-Sun rms contrast, more representative of the contrast in the whole frame and not only close to the lock point, is that provided by a blob finding algorithm (see Tritschler & Uitenbroek 2006). We use this algorithm to locate G-band bright points and eliminate the pixels encompassed by them from the rms estimate. The resulting rms values are plotted with the solid curve and filled circles in the bottom panel of Figure 3. In general the two estimates for the quiet-Sun rms contrast match each other very well.

Typically, the reconstruction process raises the rms contrasts in the images by about a factor of two, to typical values of between 7 and 14%, with the highest contrast over the whole image as recovered with the blob algorithm at values close to this upper bound. The contrast of the reconstructed images is highly correlated with the contrast of the burst images. During "bad seeing" (as judged by the correspondingly low values of  $r_0$  in Figure 2, *top panel*) high spatial frequency information is lost and cannot be recovered by the reconstruction algorithm. Otherwise, the reconstructed contrast would be consistently close to 14%. The upper limit is reached for a range of "input image contrasts" of 7-9%. This means the reconstructed contrast saturates, which can only be expected if the spatial power spectrum of the granulation does not have a high frequency tail at spatial scales below the resolution limit of the telescope.

With the doubling of the rms contrast, the improvement in image quality is clearly illustrated by the sample images in Figure 4. The figure shows, from right to left, the central part of a frame representing the average over the 80 exposures in one burst (number 15, with the highest average contrast in individual exposures and in the reconstructed image of the burst), the reference frame for the reconstruction (the image with the highest contrast within the burst), and finally the reconstructed image.

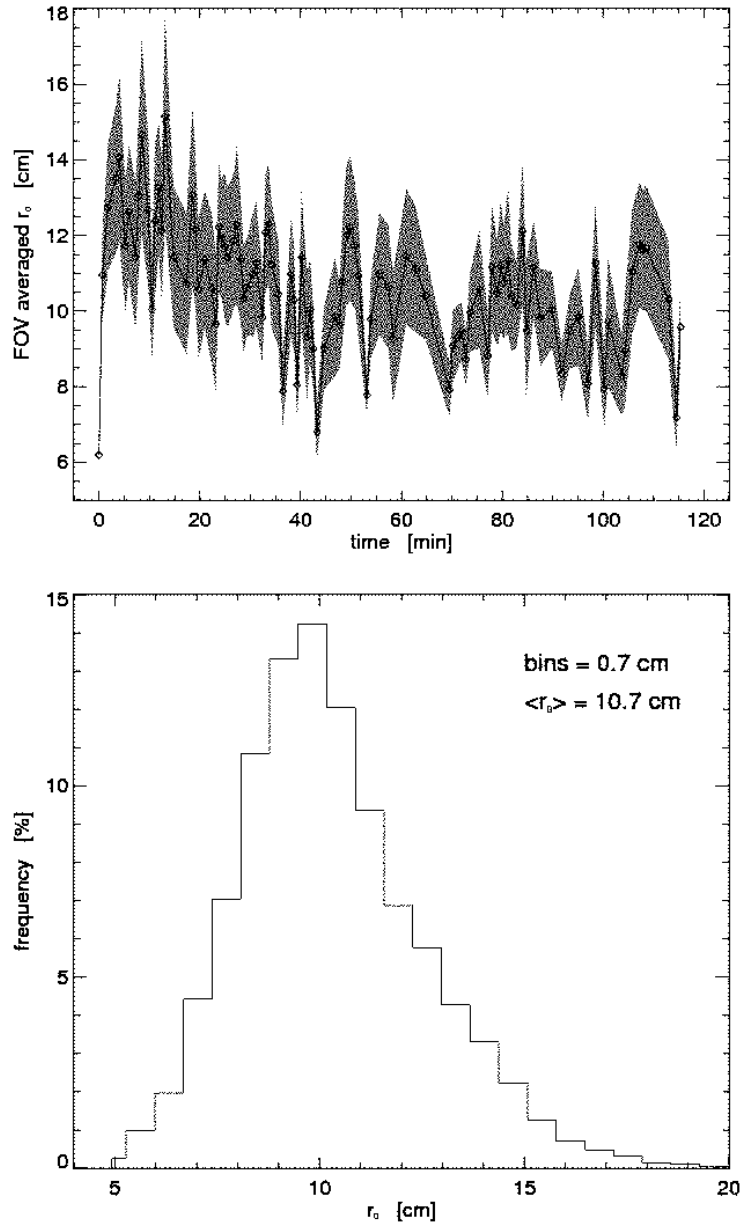


Fig. 2.— The average Fried parameter  $r_0$  over the FOV, as determined for each burst by the speckle reconstruction code is shown in the *top panel*, together with its standard deviation (gray shading). The *bottom panel* shows the histogram of  $r_0$  values determined by the speckle code for all  $15 \times 15$  subfields in all bursts.

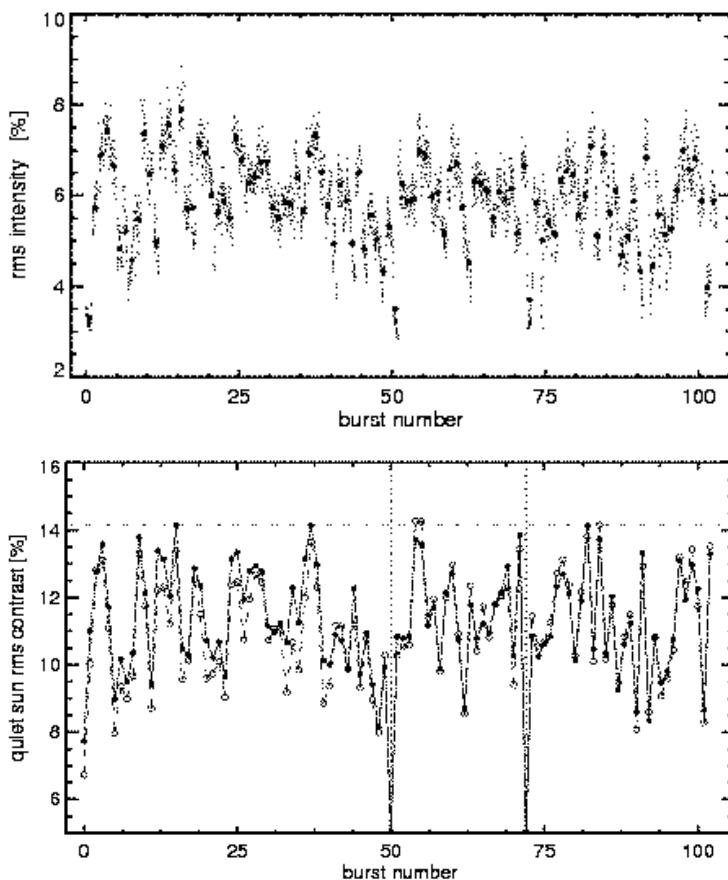


Fig. 3.— Rms contrast variation in the individual frames for all 103 bursts (*top panel*). Vertical gray lines indicate the start of each successive burst. *Bottom panel* shows the quiet-Sun rms contrast of all reconstructed frames, measured from the contrast in a subarea (indicated by the white rectangle in Figure 1, *dashed curve and open circles*), and from the blob algorithm (see text, *solid curve and filled circles*). The maximum rms (14.1%) in the reconstructed images derived with the latter is indicated by the horizontal dashed line. The vertical dotted lines indicate the two bursts for which the iterative reconstruction failed to converge (burst 50 and 72).

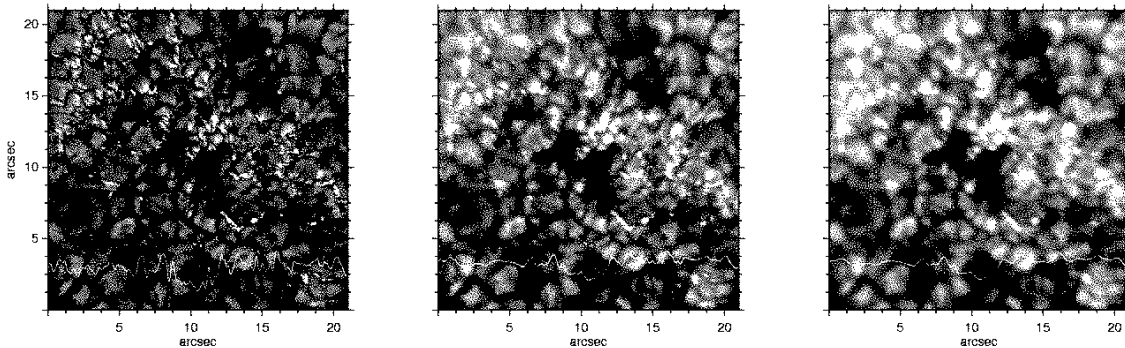


Fig. 4.— Average (*right panel*), reference (*middle*), and reconstructed (*left*) images of the central part of the field-of-view centered on the adaptive optics lock point of burst No. 15. The curve at the bottom of each image represents the G-band intensity in a cross section of the image through the pore at  $y = 9.9$  arcsec. It illustrates the recovery of the amplitude of high spatial frequencies in the reconstructed images.

#### 4. Simulations

We compare the speckle reconstructed G-band images with intensities obtained from two different simulation snapshots that span a realistic range in average field strengths on the solar surface outside sunspots. The first one, here referred to as quiet-Sun has an average vertical magnetic field of 30 G, which is probably at the lower limit of what can be expected in real quiet-Sun areas (Trujillo Bueno et al. 2004). The second snapshot is representative of solar plage with an average vertical field of 250 G. It will be referred to as the plage snapshot. Both snapshots were taken from magneto-hydrodynamic simulations by Stein & Nordlund (2006). We employ carbon and oxygen abundances of  $\log \epsilon_C = 8.39$  and  $\log \epsilon_O = 8.66$ , respectively as advocated by Asplund et al. (2005) on the basis of C I, CH, and C<sub>2</sub> line modeling in three-dimensional hydrodynamic simulations, and similar modeling by Asplund et al. (2004) of O I and OH lines, and CO lines Scott et al. (2006). The precise value of the oxygen is relevant for the opacity in the G band region because most carbon in the cool parts of the solar atmosphere is bound in CO molecules limiting the amount available for CH.

A description of the spectral synthesis is given in (Uitenbroek & Tritschler 2006). For each of the two snapshots the emergent spectrum in the G-band region was calculated at 600 wavelengths equidistantly spaced over a range of 3 nm centered at 430.5 nm. In the computation this wavelength interval contains 356 atomic lines and 424 electronic molecular transitions of the CH A<sup>2</sup>Δ–X<sup>2</sup>Π system with vibrational quantum numbers  $v - v' = 0 - 0$ ,  $1 - 1$ , and  $2 - 2$ . The calculated spectra were then integrated over a typical G-band filter function of 1 nm FWHM with the shape of a second order generalized Lorentzian, representative of a dual-cavity interference filter. The rms

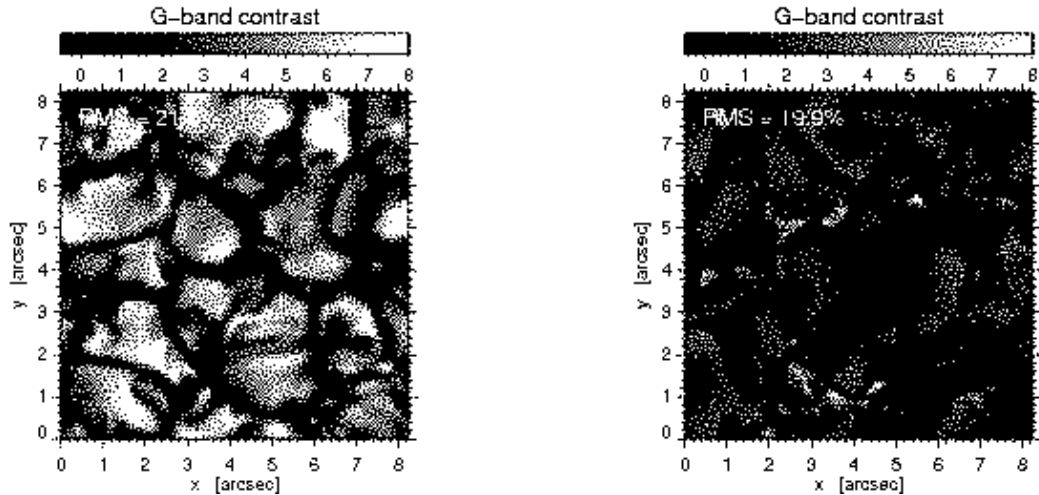


Fig. 5.— Synthetic G-band filtergrams from quiet-Sun (*left panel*) and plage (*right panel*) snapshots. Indicated in white are the rms contrast variations over the whole filtergrams, and indicated in grey lettering the rms contrast of pixels outside bright points in the plage snapshot.

intensity differences of the spatially averaged spectrum from the snapshots with the observed average solar spectrum are only 7% over the 3 nm spectral range (Uitenbroek & Tritschler 2006), confirming the realism of the synthetic spectra. The main differences between computed and observed spectra result from slight differences in the central wavelengths of the included spectral lines. These intensity differences are inconsequential to the wavelength integrated G-band signal.

Synthetic filtergrams of the two simulation snapshots as well as the values of their respective rms contrast in the G band are shown in Figure 5. The plage snapshot (*right panel*) includes concentrations of magnetic field in its inter-granular lanes that are strong enough to give rise to G-band bright points, while this not the case anywhere in the quiet-Sun snapshot, despite the presence of a 30 G average vertical field. As a result of the bright points the range in contrasts in the plage snapshot is much higher, and the overall rms contrast is raised as well (see also Tritschler & Uitenbroek 2006, table 2 therein). However, the contrast of the plage snapshot measured in the granulation alone, after eliminating pixels in bright points, is much reduced compared to the quiet Sun due to the presence of the stronger magnetic field, which inhibits convective flows, and hence heat advection. The granular rms contrast is only 16.3% compared to 21.5% in the quiet-Sun snapshot (see annotations in grey and white, respectively in Figure 5), keeping in mind that the former number is a slight underestimate because the inter-granular lanes are underrepresented in the rms through the elimination of bright-point pixels, which occur preferentially in the dark lanes.

## 5. Comparison of observed and theoretical G-band contrasts

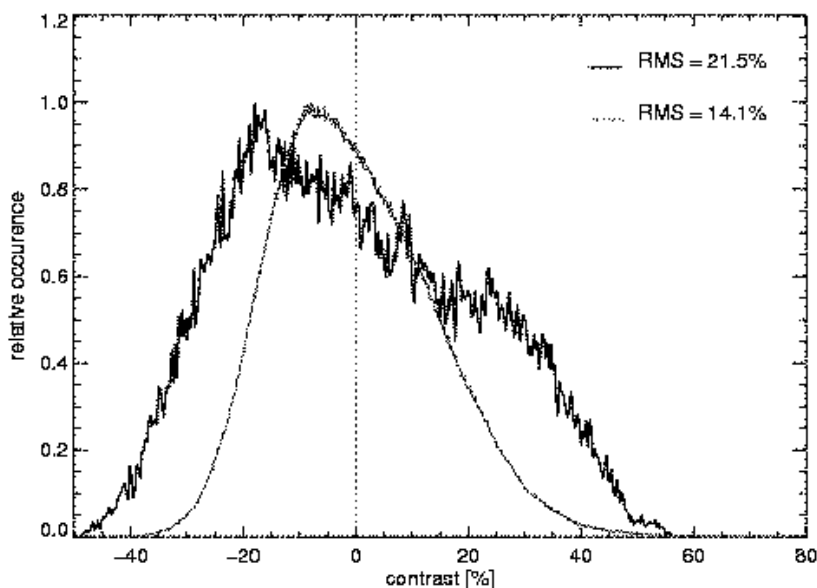


Fig. 6.— Histograms of G-band contrast values in the synthetic quiet-Sun filtergram (*grey curve*) and best reconstructed image (No. 15, *black curve*).

Comparing the rms contrast values between the synthetic filtergrams and the values for the reconstructed images (Figure 3, *bottom panel*) the large differences are obvious. Where the simulations have a granular rms contrasts of 21.5% for quiet Sun, the highest contrast in the most quiet regions of the observed reconstructed G-band images is 14.1%. This difference is further exemplified in the comparison of histograms of contrast values in the synthetic quiet-Sun filtergram (*black curve*) and the reconstructed frame with the highest contrast (from burst No. 15, *gray curve*). The reconstructed image lacks both relatively dark pixels with contrasts less than  $-30\%$ , and relatively bright pixels, with excess contrast of  $+30\%$  compared to the synthetic filtergrams. In addition, the histogram of the synthetic filtergram is more clearly a bimodal distribution of two Gaussians with a main peak at  $-20\%$  and a secondary peak at  $+25\%$ . The histogram of the observed filtergram can also be closely represented by a sum of two Gaussian distributions, but with maxima that are much closer zero, giving the impression of a unimodal rather than a bimodal distribution.

The darkest (contrast less than  $-0.30$ , white contours) and brightest features (contrast less than  $+0.30$  black dashed contours) in the synthetic quiet-Sun snapshot are outlined in Figure 7. Clearly, the dimensions of the darkest and brightest areas in particular are well above the theoretical resolution limit of the DST (which is  $0''.117$  at the central wavelength of the G band), and should be resolvable in the speckle reconstructed images when seeing is good. This suggests that the

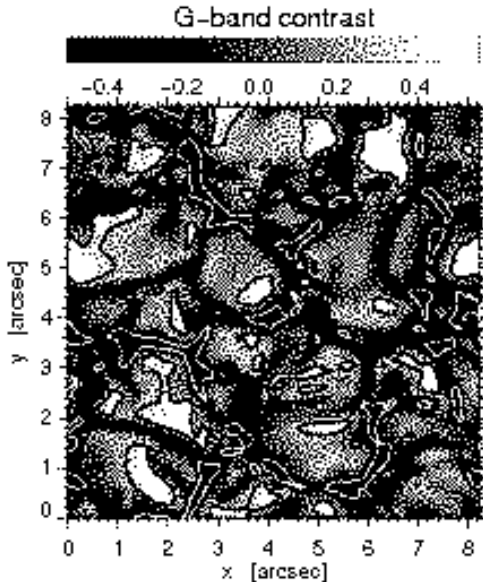


Fig. 7.— Contours outline the pixels with contrasts of less than  $-30\%$  (*white contours*), and more than  $+30\%$  (*black contours*).

properties of the simulation we designate as quiet-Sun are inherently different from the real quiet Sun. In turn this implies that temperature fluctuations in the simulations are overestimated because granular intensities in the G-band filter signal are dominated by the continuum and are directly related to temperature at heights between 25 – 50 km. (Uitenbroek & Tritschler 2006).

To verify that the quiet-Sun simulation snapshot does not represent an exceptional case of rms high contrast, we investigated the statistics of rms contrast of subfields of comparable size in the observations. A histogram of rms contrast values in  $8''.5 \times 8''.5$  subfields of the 101 successfully speckle-reconstructed images is shown in Figure 8. Only 0.89% of the subfields have a rms contrast of 14.1% (the highest value of rms in the quiet area of the reconstructed frames), and only 0.01% has an rms of 20% or more. It is therefore highly unlikely that the simulation snapshot we employed happens to correspond to the high contrast tail of the distribution of subfield rms values. At first sight it seems questionable that less than 1% of subfields have rms contrast more than 14.1%, since there are several frames with quiet-Sun rms contrast that high (see Figure 3, *bottom panel*). The explanation for this seeming discrepancy is the 5-minute oscillation, which has patches of intensity variation of typical size  $10''-15''$ . Such large patches contribute much more to the overall rms in the frames than to the rms contrast in subfields smaller than  $10''$ .

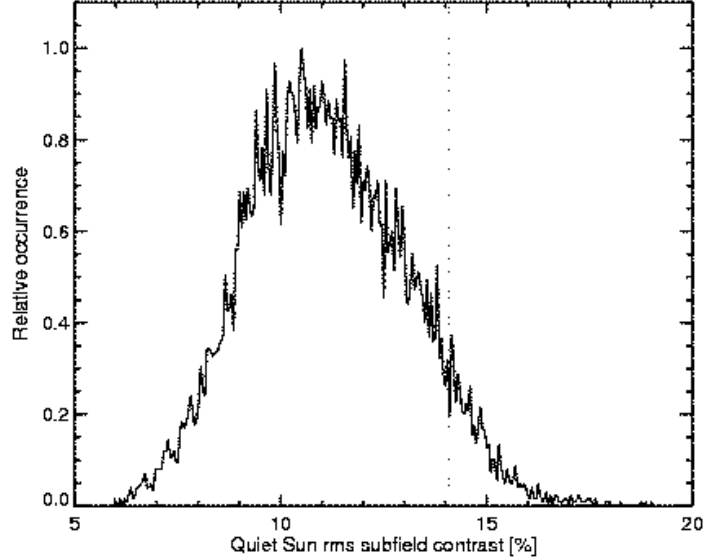


Fig. 8.— Histogram of rms contrast variation over  $8''.5 \times 8''.5$  subfields in the quiet-Sun are of the reconstructed images.

### 5.1. Spatially unresolved scattered light

One type of image degradation that reconstruction techniques do not have a handle on is the effect of spatially unresolved scattering, essentially the image smearing that occurs because of the broad outer wings of the point spread function (PSF) of the telescope and atmosphere. Is this perhaps the main reason for the substantially lower contrast of the reconstructed images with respect to the synthetic filtergrams? Below we present a simple argument that this is very unlikely the case.

Let  $I_{ij}$  the intensity in a synthetic solar image and  $\langle I \rangle = \frac{1}{N} \sum_{ij} I_{ij}$  its average over the  $N$  pixels of the image. The rms contrast  $C$  of the intensity is defined as:

$$C = \sqrt{\frac{\sum_{ij} (I_{ij} - \langle I \rangle)^2}{\langle I \rangle^2 N}}. \quad (1)$$

In the simplest approximation scattering takes a fraction  $\alpha$  of the spatially resolved intensity and spreads it equally over all pixels. The resulting degraded image  $I'$  can therefore be written as  $I' = (1 - \alpha)I + \alpha\langle I \rangle$ , with  $\langle I' \rangle = \langle I \rangle$ . The rms contrast of the degraded image is

$$C' = \sqrt{\frac{\sum_{ij} (I'_{ij} - \langle I' \rangle)^2}{\langle I' \rangle^2 N}} = (1 - \alpha)C. \quad (2)$$

For the calculated contrast to be degraded from the nominal 21.5% to the observed contrast in the best reconstructed images of 14.1% requires a scattering coefficient  $\alpha$  of at least 0.34. This is unrealistically high for the DST by at least a factor of three, as is judged from observations off the solar limb, and a transit of the planet Mercury (Reardon, private communication).

## 6. Conclusions

We have compared the rms intensity contrast in the G-band in a series of speckle reconstructed images obtained at the  $D = 0.76$  cm DST with that in two synthetic G-band filtergrams computed from magneto-hydrodynamic snapshots representative of quiet-Sun and plage with average vertical magnetic fields of 30 G and 250 G, respectively. We find that the rms G-band contrast in the best speckle-reconstructed images is just over 14%, as judged from a quiet subarea, relatively devoid of bright points, and from the overall contrast in the image after removing bright points (Figure 3, *lower panel*). This observed rms contrast is considerably lower, by more than 50%, than the rms contrast in the synthetic quiet-Sun filtergram which was found to be 21.5%. In the plage snapshot the rms contrast of the granulation, excluding pixels with bright points, is 16.3%.

The employed speckle reconstruction algorithm accounts for the effect of the telescope’s AO system, and provides reliable photometry in the reconstructions. During moments of consistently good seeing over the duration of an 80 frame speckle burst (corresponding to typical values of the Fried parameter  $r_0$  of 12 cm or larger, compare Figures 2 and 3, *top panel*), the reconstructed rms contrast seems to saturate to 14.1%, suggesting this approaches the contrast on the real Sun. To verify the conclusion that the rms G-band in the observed quiet Sun is indeed substantially different from the that in the synthetic snapshot we convolved the latter first with the telescope Point Spread Function (PSF) appropriate for the  $D = 0.76$  m DST, and then with a PSF representative for telescope plus  $r_0 = 15$  and  $r_0 = 10$  cm seeing. The resulting rms contrasts were 19.3%, 16.8%, and 14.9%, respectively. These values are again more than 50% higher than the rms contrast in the best quiet-Sun subarea in the uncorrected single frames (Figure 3, *top panel*), which do not reach more than 9%, even though they are estimated close to the AO lock point. Remarkably, the rms contrast of the quiet-Sun synthetic filtergram, degraded to the values representative of far from superior seeing (i.e.,  $r_0 = 10$  cm), is higher than that in the best reconstructed images, which should have all image degradation, apart from spatially unresolved scattering, taken out.

Areas in the synthetic filtergram with negative contrast in excess of that in the observed quiet Sun are found in the inter-granular lanes, those with positive excess in relatively large (several tenths of arcsec) patches in the granules (see Figure 7). The spatial scales of these areas are large enough, for positive excess in particular, so that they should be resolved in the best speckle reconstructed images. The synthetic filtergram, therefore, does not show significant power that

contributes to the rms at spatial scales smaller than the resolution limit of the DST, which is  $0''.117$  in the G band. The saturation of the reconstructed rms contrast to just above 14% during the moments of best seeing seems to confirm that no significant power is present in the solar granulation at spatial frequencies close to the resolution limit of the telescope. The simple consideration of degradation of contrast by spatially unresolved scattered light presented in Section 5.1 shows that it is very unlikely the cause of the discrepancy between computed and observed G-band contrasts. We remark that, given the typical spatial scale of intensity fluctuations caused by the 5 min oscillations, the latter contribute more to the rms of the large FOV spanned by our images than to the rms contrast in small fields like our simulation snapshots, which are smaller than those  $p$ -mode spatial scales. Therefore, the discrepancy in G-band contrast caused by convective motions alone is even larger than it seems from our estimates. We conclude that there remains a clear and unresolved difference between the simulated and observed rms G-band contrasts: the quiet-Sun simulation snapshot overestimates the rms G-band contrast by as much as 50%. This raises the fundamental question whether the simulations still lack fundamental physics or sufficient numerical resolution, or whether we do not fully understand the degradation of contrast by the earth atmosphere and telescope during observations.

One possible source of the contrast discrepancy is the absence of cooling by CO molecules in the simulation, where radiative transfer is approximated by only four opacity bins, and four directions. CO is the dominant coolant above the photospheres of cool stars Ayres & Testerman (e.g., 1981), and its presence may well reduce temperature differences in that layer, leading to a reduction in rms contrast variation in the G band since the latter is directly related to temperature variations at about 25-50 km above the photosphere. However, the temperature reduction by CO may only be important in layers that are higher than that (Scott et al. 2006).

The clearest hint, however, towards a solution to the G-band contrast discrepancy comes from the much reduced granular contrast in the plage simulation snapshot. Clearly, the presence of high concentrations of magnetic field inhibits convective motions and convective heat transport, and reduces temperature differences and thereby, G-band contrast. The findings described by Asensio Ramos et al. (2006) that simulated profiles of the Fe I 709.0 nm line in a purely hydrodynamic simulation Asplund et al. (2000a) show high velocities in excess of  $\pm 1.2 \text{ km s}^{-1}$  that are lacking in high resolution observed quiet-Sun observations confirms that such simulations without magnetic field seem to overestimate convective flow velocities. We speculate that the real quiet Sun contains much more magnetic field than the average 30 G that we assumed in our “quiet-Sun” snapshot, so that the comparison of its rms G-band contrast to that in the observed quiet-Sun is not appropriate, much like comparing apples to oranges. This magnetic field has to be present mainly in the form of weak fields, since it does not show up in the form of bright point in the G band. We further speculate that, if indeed the real Sun contains more magnetic field and if convective flow speeds are less than what is derived from field-free simulations, the element abundances that are

derived from such simulations are underestimated. For slower convective flows abundances would have to be increased to match the observed widths of lines. This would alleviate, at least in part, the conflict that exists between the low abundances of oxygen and carbon (Asplund et al. 2005, 2004; Scott et al. 2006), derived from three-dimensional simulations compared to their meteoritic values, and the conflict these low values pose with current models of the solar interior (eg., Ayres et al. 2006).

For more detailed comparison between observed and simulated G-band contrast more simulations are required with intermediate field strengths between the 30 G and 250 G average values we employed here. In addition, observations from space, where the degradation of image quality by the earth atmosphere is eliminated, and only the easier to characterize contrast reduction caused by the telescope and instrument has to be considered, should conclusively establish the value of the G-band contrast of the real Sun, hopefully confirming our conclusions here. This has to be accompanied by deep measurements of the magnetic (vector) field, so that we can finally answer the question what really constitutes quiet Sun.

We are grateful to Bob Stein for providing the simulation snapshots, and to Friedrich Wöger for allowing us to use his speckle reconstruction code.

## REFERENCES

- Asensio Ramos, A., Janssen, K., Cauzzi, G., & Reardon, K. 2006, *Memorie della Societa Astronomica Italiana Supplement*, 9, 59
- Asplund, M., Grevesse, N., Sauval, A. J., Allende Prieto, C., & Blomme, R. 2005, *A&A*, 431, 693
- Asplund, M., Grevesse, N., Sauval, A. J., Allende Prieto, C., & Kiselman, D. 2004, *A&A*, 417, 751
- Asplund, M., Ludwig, H.-G., Nordlund, Å., & Stein, R. F. 2000a, *A&A*, 359, 669
- Asplund, M., Nordlund, Å., Trampedach, R., Allende Prieto, C., & Stein, R. F. 2000b, *A&A*, 359, 729
- Ayres, T. R., Plymate, C., & Keller, C. U. 2006, *ApJS*, 165, 618
- Ayres, T. R., & Testerman, L. 1981, *ApJ*, 245, 1124
- Keller, C. U. 2007, in H. Uitenbroek, J. Leibacher, R. F. Stein (eds.), *Astronomical Society of the Pacific Conference Series Vol. 354*, p. 3

- Matson, C. L. 1991, *Journal of the Optical Society of America A*, 8, 1905
- Rimmele, T. R. 2004, in D. Bonaccini Calia, B. L. Ellerbroek, R. Ragazzoni (eds.), *Advancements in Adaptive Optics*. Edited by Domenico B. Calia, Brent L. Ellerbroek, and Roberto Ragazzoni. *Proceedings of the SPIE*, Volume 5490, pp. 34-46 (2004)., p. 34
- Schaffnerberger, W., Wedemeyer-Böhm, S., Steiner, O., & Freytag, B. 2006, in H. Uitenbroek, J. Leibacher, R. F. Stein (eds.), *Astronomical Society of the Pacific Conference Series Vol. 354*, p. 345
- Scott, P. C., Asplund, M., Grevesse, N., & Sauval, A. J. 2006, *A&A*, 456, 675
- Stein, R. F., & Nordlund, Å. 1998, *ApJ*, 499, 914
- Stein, R. F., & Nordlund, Å. 2000, *Sol. Phys.*, 192, 91
- Stein, R. F., & Nordlund, Å. 2006, *ApJ*, 642, 1246
- Tritschler, A., & Uitenbroek, H. 2006, *ApJ*, 648, 741
- Trujillo Bueno, J., Shchukina, N., & Asensio Ramos, A. 2004, *Nature*, 430, 326
- Uitenbroek, H., & Tritschler, A. 2006, *ApJ*, 639, 525
- Vögler, A., Shelyag, S., Schüssler, M., Cattaneo, F., Emonet, T., & Linde, T. 2005, *A&A*, 429, 335
- van Noort, M., Rouppe van der Voort, L., & Löfdahl, M. G. 2005, *Sol. Phys.*, 228, 191
- von der Luehe, O. 1993, *A&A*, 268, 374
- Wöger, F. 2007, *High-resolution observations of the solar photosphere and chromosphere*, Ph.D. Thesis University of Freiburg, Germany, <http://www.freidok.uni-freiburg.de/volltexte/2933/>